

On the build-up of effective hyperuniformity from large globular colloidal aggregates

Antonio Díaz-Pozuelo¹ and Diego González-Salgado², and Enrique Lomba¹

¹Instituto de Química Física Blas Cabrera, CSIC, Calle Serrano 119, E-28006 Madrid, Spain

²Modelización y Simulación de Materiales Nanoestructurados, Universidad de Vigo, Unidad Asociada al CSIC por el IQF, Departamento de Física Aplicada, E-32004, Ourense, Spain

Abstract. A simple three-dimensional model of a fluid whose constituent particles interact via a short range attractive and long range repulsive potential is used to model the aggregation into large spherical-like clusters made up of hundreds of particles. The model can be thought of as a straightforward rendition of colloid flocculation into large spherical aggregates. We illustrate how temperature and particle density influence the cluster size distribution and affect inter- and intra-cluster dynamics. The system is shown to exhibit two well separated length and time scales, which can be tuned by the balance between repulsive and attractive forces. Interestingly, cluster aggregates at moderate/low temperatures approach cluster glassy phases whereas the clusters itself are liquid droplets. These states present a strong suppression of density fluctuations for a significant range of relatively large wavelengths, meeting the criterion of effective disordered hyperuniform materials.

1. Introduction

Spontaneous pattern formation and self-limiting association can be deemed key phenomena both in biological and soft matter physics [1]. In the former, colloidal suspensions are characteristic examples in which a variety of patterns have been identified in systems as disparate as amphiphilics [2], proteins such as lysozyme [3] or antibodies [4] (see Kovalchuk and coworkers [5] and references therein for a more comprehensive review of experimental examples). As a particularly interesting illustration of self-limiting aggregates, recently Sweatman and Lue [6] have argued that the formation of giant clusters due to the competition between attractive and repulsive interactions might well be behind the condensation of proteins/nucleic acids into membraneless organelles within the nuclei of eukaryotic cells [7]. This is an alternative view to the “traditional” liquid-liquid phase separation picture that is common among the structural biology community [8].

As to pattern formation in soft matter systems, there is a growing interest on this subject, in particular for the possibilities that non-templated thermodynamically controlled nano-patterning [9–11] offers in the field of nanotechnology. In this connection, simple models that exhibit short range attraction and long range repulsion (SALR), [12,13] have shown to be able to reproduce the experimental behavior in great detail. In the pioneering work of Andelman and coworkers it was predicted by means of a mean field theory that, for a sufficiently large amplitude of repulsive interactions, modulated cluster phases will emerge [14]. The central role of attraction/repulsion competition in the build-up of globular bubble cluster, and ordered modulated phases or bicontinuous percolating clusters that span up to macroscopic sizes, has been known for more than three decades [13]. The shape and size of the clusters and their spatial organization is directly determined by the balance between attractive and repulsive forces, as shown by the ground state calculations of Mossa et al. [15]. Obviously, thermodynamic conditions (density and temperature/pressure) play a key role as well. Recently Liu and Xi [16] proposed a classification of SALR potentials in terms of the ratio between repulsive and attractive forces and particle size. Thus SALR potential are classified into type-I (range of the attraction is less than 20% of the particle size, and range of the repulsion is a fraction of the particle size), type-II (range of the attraction less than 20% of the particle size, range of repulsion is comparable or larger than particle size) and type-III (range of attraction beyond 20% of particle size and range of repulsion as in type II). In Ref. [16] it was shown that these three classes of interactions lead to specific features as to their phase behavior and cluster morphology.

The phase behavior of SALR systems has been dealt with extensively using theoretical [14,17–21] and simulation approaches [22–24]. A comprehensive summary of relevant contributions in this connection can be found in recent review works [16,25,26]. It should be stressed that in all these instances, the long range repulsive component of the interaction is essential for the self-limitation of the aggregation process, preempting condensation/demixing transitions. The latter would drive the system towards spatially

separate macroscopic phases [24] instead of the microstructuring induced by clustering. It is worth mentioning that other alternative approaches can explain self-limitation in aggregation processes as well. Such is the case, for instance, when the presence of specific interactions in mixtures limits the growth of the aggregate due the saturation of bonding sites by one of the components [27], in parallel with the chain termination in radical polymerization reactions.

Finally, as stated by Klix and coworkers [23] SALR systems are intrinsically frustrated, and this also affects their dynamics, which is mostly controlled either by mesoscopic order or by metastable disorder [23]. These authors actually identify three dynamically arrested phases in their SALR model with long range electrostatic repulsions: a Wigner glass (moderate packing fraction/weak attractive interactions), a cluster glassy state (low packing fraction, strong attractive interactions), and a percolating gel phase (high packing fraction/strong attractive interactions). The possibility of the existence of a Wigner glass phase in disordered systems with long range electrostatic interactions was first postulated by Bose and Wilke using mode coupling theory [28]. Dawson et al [29] further analyzed in detail the possibility of dynamically arrested states in colloids stemming from either attractive or repulsive forces, whose ratio, as Klix et al. [23] have shown, controls both the type of dynamics and topology of the glassy states.

Experimental evidence of colloidal glassy states is extensive and, for instance, numerous examples can be found in the review chapter by Weitz [30]. These glassy states are particularly interesting from the technological standpoint, since they provide an avenue to manufacture a wide range of solid-like materials starting from colloidal solutions, and as will be shown in this work, they offer a feasible alternative for the fabrication of disordered hyperuniform materials. These systems are exotic states, lying in between crystals and fluids [31, 32], i.e. while being structurally disordered, they exhibit a hidden order, that in common with crystalline order suppresses large scale density fluctuations. Aside from its ubiquitous occurrence in physical and biological systems (cf. see Ref. [32] for a comprehensive review of the multiple systems in which disordered hyperuniformity is present), hyperuniform materials have been shown to display particularly interesting optical [33–37] and acoustic properties [38, 39]. Manufacturing hyperuniform materials from colloidal aggregates opens multiple paths to the fine tuning of their optical/acoustical properties, since in addition to the aggregate composition (and corresponding form factor of the constituent particles), the size and/or topology of the particulate aggregates can also be controlled by chemical and physical means.

In this article we will revisit a particularly simple model of colloidal SALR system that can yield all types of cluster phases, and ultimately will be shown to be capable of producing disordered effective hyperuniform states. The two dimensional version of this model was explored in detail two decades ago by Imperio and Reatto [40–43]. The model, in which both attractive and repulsive interactions are simple exponentials, i.e. Kac interactions [44], was initially introduced in this context by Sear and coworkers [9]

to account for the spontaneous patterning of quantum dots at the air-water interface. Later, Archer and coworkers [14, 18, 22] used density functional theory and extensive Monte Carlo simulations in a three-dimensional version of the same model, in order to explore its phase behavior and map its corresponding phase diagram. Schwanzer and Kahl [45] analyzed the competition between clustering and vapor liquid condensation, and the cluster/particle dynamics [46] again in two dimensions. Interestingly, the same Kac-potential model was also used by Meyra and coworkers [49, 50] to explain the formation of vegetation patterns in environments with limited resources. This illustrates how SALR effective interactions can provide a qualitative (and even quantitative) explanation for spontaneous patterning over various orders of magnitude in the spatial (and to some extent temporal) dimension. In addition to all these studies in the bulk, Bores et al. [47, 48] performed simulations and theoretical studies on the influence of confinement into disordered media on the pattern formation for the same SALR model in two dimensions as well.

In the comprehensive work of Archer and Wilding [22], in addition to the vapor-liquid transition, two first order transitions were identified depending on the packing fraction. Namely, a phase change at high dilution between a vapor and a fluid of liquid-like spherical clusters (globular cluster phase), and another transition between a liquid and fluid of spherical voids (bubble cluster phase). In this paper we will focus solely on the first instance, with interaction parameters and thermodynamic conditions tuned to yield relatively large clusters. Here, using large scale simulations we have analyzed the cluster size distributions, the intercluster and intracluster microscopic structure and dynamics illustrating their dependence on the thermodynamic conditions. In contrast with the two-dimensional model, in which as temperature is lowered both the intracluster and intercluster structure rapidly freeze into hexagonal arrangements, the three-dimensional system retains the liquid-like structure of the cluster droplets, and the freezing of intercluster structure is frustrated, with the system displaying features characteristics of a glass. It is worth recalling that after the freezing in 2D, the hexagonal lattice structure does not constitute a proper infinite crystal, since thermal fluctuations destroy long range orientational order, while retaining only long range bond orientational order [51]. In this work, we will exploit the long range of the net inter-cluster interactions and relatively large attractive interparticle interaction (a type-III SALR potential), to find the conditions in which clusters end-up in the vicinity of a dynamically arrested state, a cluster glassy phase [23]. We will see that the second peak of the cluster-cluster pair distribution function exhibits a splitting which is a characteristic feature of dense amorphous materials (e.g metallic glasses [52]). It will be shown that these states display a strong attenuation of density fluctuations for a significant region of small wavenumbers, which is apparent in the large wavelength behavior of the cluster-cluster structure factor. The system then effectively resembles a stealthy disordered hyperuniform material [31, 53, 54], i.e. due to the suppression of density fluctuations for a certain region of large wavelengths, the material becomes to some extent “invisible” to the corresponding radiation probes.

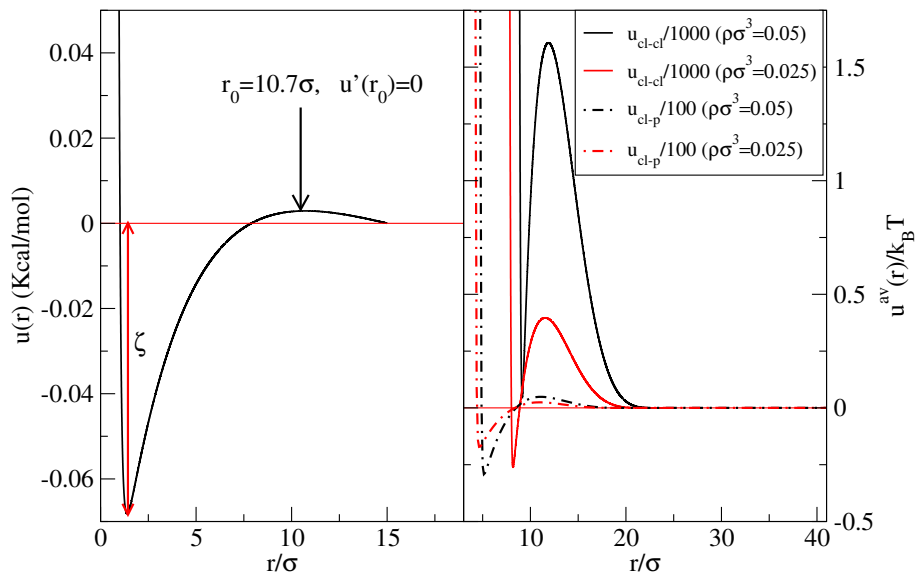


Figure 1. Left) SALR interaction potential as described by Eq. (3). Right) Average intercluster potential (solid curves) and cluster-particle potential (dashed curves), computed assuming an uniform average cluster density and spherical cluster radii.

The presence of an additional region with some attenuation for much shorter wavelengths (reflecting intracuster correlations) indicates that, to a smaller degree, it might be possible to have some sort of “stealthiness” for higher frequencies. As long as one can tune intracuster (i.e. particle-particle) correlations and/or composition this opens new possibilities for this type of materials.

The rest of the paper is sketched as follows. In the next section we will describe the SALR model and the simulation conditions. The single cluster structure (cluster size distributions, density profiles, average life times) and dynamics will be reviewed in Section 4. Two-particle and intercluster correlations, together with the build up of disordered hyperuniformity are commented upon in Section 5. The article is closed with a summary of our most relevant conclusions and future prospects.

2. Model and methods

As mentioned in the Introduction the particles in our model will be interacting via a two-exponential Kac potential of the form used in Refs. [9, 14, 19, 22, 40, 47] to which we have added a soft core as in Ref. [47] in order to facilitate the use of molecular dynamics, namely

$$u^{SALR}(r) = \varepsilon \left[K_r e^{-\alpha_r r/\sigma} - K_a e^{-\alpha_a r/\sigma} + \left(\frac{\sigma}{r}\right)^{10} \right]. \quad (1)$$

Here σ is a measure of the inner particle core diameter and will be used as unit length. Since this is a rather soft potential, the actual size, as estimated from the particle-particle

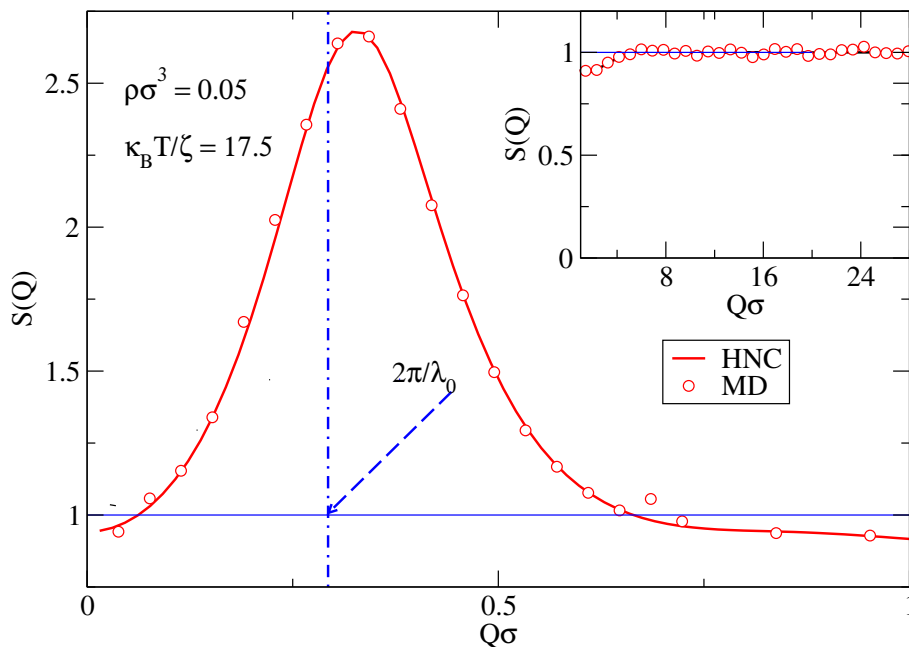


Figure 2. High temperature structure factor from our HNC calculations (lines) vs MD results (symbols). In these conditions the system is in the homogeneous phase displaying the initial formation of aggregates. A vertical line marks the position of $2\pi/\lambda_0$,

distribution function is $\sigma_{eff} \approx 0.8\sigma$. As mentioned by Sear and coworkers [9], while the use of the attractive exponential can be justified as a more or less crude modelization of dispersive forces as in the classical works by Kac et al. [44,55], the repulsive exponential is used solely for the sake of computational simplicity. Thus, with $K_a, K_r > 0$, and $\alpha_a > \alpha_r > 0$ one has the characteristics of a SALR potential with the presence of a maximum for a distance r_0 , larger than that corresponding to the potential minimum, and whose analytical expression reads

$$r_0 = \frac{\sigma}{\alpha_a - \alpha_r} \log \frac{\alpha_a K_a}{\alpha_r K_r}. \quad (2)$$

The effect of the inner repulsive core on the value of r_0 is negligible. r_0 is a very significant correlation distance that in the case of globular clusters roughly determines the cluster size. As will be explained below, due to the long range character of the interaction, the average intercluster distance is twice as large, i.e. $\lambda_0 = 2r_0$. For lamellar phases, λ_0 determines the modulation distance, and in the bubble phase the average distance between the bubbles. In all cases the signature of this correlation length, λ_0 , is the presence of high intensity peak in the structure factor, $S(Q)$, located at $Q_m \approx 2\pi/\lambda_0$. For computational convenience the potential has been truncated and shifted at $R_c = 60\sigma$, i.e., we will be dealing with an interaction given by

$$u(r) = \begin{cases} u^{SALR}(r) - u^{SALR}(R_c) & \text{if } r \leq R_c \\ 0 & \text{if } r > R_c \end{cases} \quad (3)$$

Setting $K_r = 1$ and $K_a = 2$, $\sigma = 4 \text{ \AA}$, $\varepsilon = 0.1 \text{ kcal/mol}$, $\alpha_r = 0.1$ and $\alpha_a = 0.25$ one gets the potential depicted in the left graph of Figure 1. With this choice of parameters $r_0 = 10.7\sigma$ which, as mentioned above, determines the cluster diameter, as will be further confirmed in the next Section when discussing the average cluster density profiles. We will consider systems at relatively low number densities in order to guarantee the formation of micellar-like phases. Two total densities will be studied, $\rho\sigma^3 = 0.025, 0.05$.

The fact that the correlation length is twice the position of the potential maximum is easily understood in the case of globular clusters. In this instance one can assume a uniform effective density, ρ_{cl}^{eff} , inside the spherical clusters of effective radius R_{cl}^{eff} . These two quantities can be considered as optimization parameters in a Reverse Monte Carlo procedure [56], in which the interaction potential is computed from

$$u_{cl-cl}^{av}(r; \rho_{cl}^{eff}, R_{cl}^{eff}) = \left(\rho_{cl}^{eff}\right)^2 \int_{V_{cl}} d\mathbf{r}_1 \int_{V_{cl}} d\mathbf{r}_2 u(|\mathbf{r} - \mathbf{r}_1 + \mathbf{r}_2|) \quad (4)$$

with the objective function being the intercluster pair distribution. We have performed these calculations for the aforementioned densities. With the temperature defined as $k_B T/\zeta$ in terms of the potential well depth, ($\zeta = 0.068 \text{ kcal/mol}$, see Figure 1), k_B being Boltzmann's constant, the cluster-cluster potentials have been evaluated for the lowest temperature considered, $k_B T/\zeta = 3$. The double volume integrals over the cluster volumes are carried out numerically using a Gauss-Legendre quadrature, with $u(r)$ given by Eqs. (1) and (3). With this procedure we end up with estimated effective cluster densities of $\rho_{cl}^{eff}\sigma^3 = 1.2$ ($\rho\sigma^3 = 0.05$) and 0.83 ($\rho\sigma^3 = 0.025$), with corresponding effective radii, $R_{cl}^{eff}/\sigma = 4.5$, and 4 , respectively. The results obtained from Eq. (4) are presented in the right graph of Figure 1. The dashed curves correspond to the cluster-particle interaction that is simply obtained by removing one of the effective cluster densities and one volume integration from Eq. (4). We see in the Figure that the net inter-cluster interaction is extremely repulsive, orders of magnitude more intense than the interparticle potential, and dies out approximately at $\lambda_0 = 2r_0$. This explains why this correlation length determines the intercluster separation, as reflected by the first peak of the cluster-cluster pair distribution that will be discussed in the next section. Note that this is not a consequence of the cut-off introduced in (3) for computational convenience since $R_c \approx 3\lambda_0$. It is the competition between attractive and repulsive components what cancels most of both the cluster-cluster and (to a lesser extent) the cluster-particle interactions at approximately λ_0 . Interestingly, our spherical clusters act like large repulsive spheres of approximate diameter λ_0 whereas their actual diameter (the precise value depends on the definition as we will see) is $\approx \lambda_0/2$, i.e. the excluded volume is 2^3 times the average cluster volume.

Molecular dynamics simulations have been run specifically in the NVT ensemble using the LAMMPS package [57] for a total of 218000 particles of mass 100 amu. Distance and energy units for the simulation have been chosen following the LAMMPS package *real* units specification. The integration time step was set to 2 fs. Results will be presented in terms of reduced units, both for temperature (defined in terms of the well

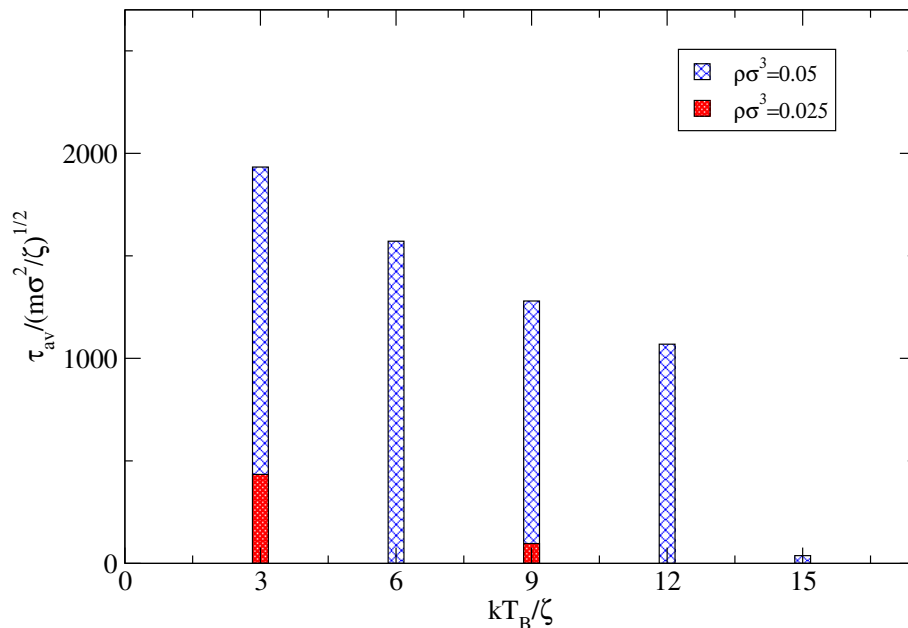
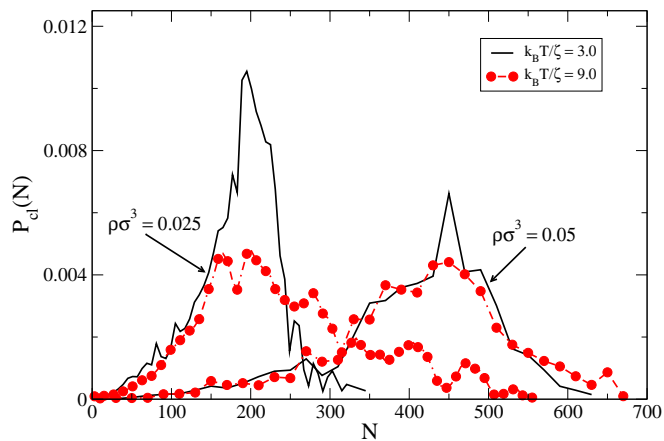


Figure 3. Average life time of the clusters, (τ_{av} , red bars) as a function of temperature for $\rho\sigma^3 = 0.05$ (blue bars) and $\rho\sigma^3 = 0.025$ (red bars). The upper limit of the y -axis corresponds to the length of the simulation production run, τ_{run} .

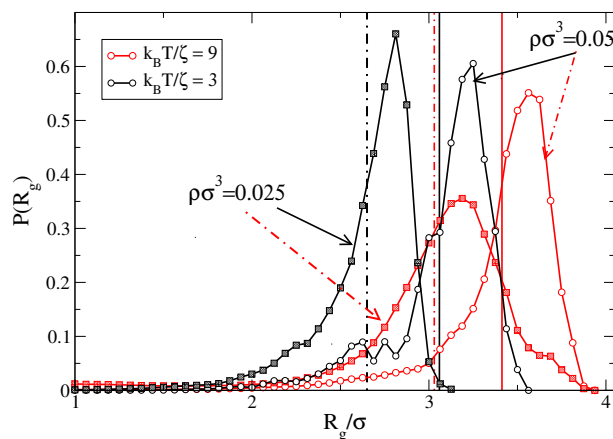
depth as indicated above), length (using $\sigma = 4\text{\AA}$ as unit length) and time, for which the reduced time unit is given by $\tau_0 = (m\sigma^2/\zeta)^{1/2} = 7.5\text{ps}$. The systems were equilibrated for 20 ns, of which the first 10 ns correspond to a slow cooling process following a linear temperature ramp starting from a fully disordered system at $k_B T/\zeta = 18$ down to the desired temperatures, namely, $k_B T/\zeta = 3, 6, 9, 12$, and 15 for $\rho\sigma^3 = 0.05$ and just $k_B T/\zeta = 3$, and 9 for $\rho\sigma^3 = 0.025$. It is worth stressing that shorter equilibration runs (5 ns) lead to very similar cluster size/radii distributions. This is an indication that the results presented correspond to equilibrium states. For much shorter equilibration runs and/or cooling times it is very easy to end up with bimodal or even multi-modal cluster size/radii distributions. Production runs were $\tau_{run} = 20\text{ns}$ long with configurations stored every 10 ps.

3. Onset of clustering

As mentioned before, we have chosen potential parameters and thermodynamic conditions for the system to yield a globular cluster phase. We have first explored a series of temperatures for the two densities indicated above using the Hypernetted Chain integral equation [58]. As shown by Archer and Wilding [22] this equation has a non-solution region which hides the cluster phase. This lack of solutions (in fact solutions have analytical continuation in the complex space [59]) can be interpreted as a signature of a phase transition, in this instance a first order transition between the particle gas and a fluid of liquid-like spherical clusters. In our case we find that real solutions for the largest density disappear below $k_B T_{ns}^{HNC}/\zeta = 14.9$, and $k_B T/\zeta = 8$



(a)



(b)

Figure 4. a) Cluster size distribution dependence on temperature and global density b) Cluster radii of gyration distribution in terms of density and temperature. Average radii are indicated by vertical lines.

for $\rho\sigma^3 = 0.025$. For $k_B T/\zeta = 17.5$ and $\rho\sigma^3 = 0.05$ the HNC converges yielding a structure factor in excellent agreement with the simulation (cf. Figure 2). A visual inspection of simulation snapshots does not show evidence of clustering. Interestingly, in Figure 2 we first see that for this temperature there is a significantly high prepeak (also known as intermediate range order peak [24]) which reaches the value $S(Q_m) \approx 2.7$ for $Q_m \approx 2\pi/\lambda_0$, whereas for $Q\sigma \gtrsim 1$ the structure factor corresponds to that of a dilute gas of uncorrelated particles. Godfrin and coworkers propose the use of this precise value of the prepeak height as signature of the onset of the cluster phase [24]. We will see in the next sections that lowering the temperature increases the height of the prepeak by orders of magnitude, i.e. $S(Q_m)$ practically diverges for a $Q_m \neq 0$, which suggests the existence of a non-zero Lifshitz point [20]. This means that the system

becomes unstable with respect to a modulated inhomogeneous phase, whose modulation is given by $Q_m \approx 2\pi/\lambda_0$. The locus of Lifshitz points for varying densities yields the λ -line [22], a term borrowed from the study of criticality in ionic fluids [60]. It must be mentioned, that Bollinger and coworkers [61] suggested the use of an additional criterion to characterize the onset of the cluster phase, namely, a thermal correlation length with values within the interval $2 \lesssim \xi_T/\sigma \lesssim 3$. This quantity can be estimated from a Lorentzian fit of the prepeak, which in our case yields $\xi_T/\sigma = 5.6$, exceeding the limit suggested in Ref. [61]. However, one must bear in mind that Ref. [61] is focused on Yukawa (screened Coulomb) interactions, and here we are dealing with bare exponentials. So far it has not been assessed to what extent the choice of the explicit form of the potential affects the reliability of this criterion. Until a complete analysis of the type performed in Ref. [61] is carried out it seems reasonable to stick to Godfrin's et al choice.

4. Single-cluster structure and dynamics

In order to define the clusters we have used a geometric criterion, namely, all those particles whose separation is below $d_{cl} = 1.3\sigma$ are considered as pertaining to the same cluster. This distance roughly corresponds to the first non-zero minimum of the particle-particle pair distribution function, i.e. it is an estimate of the outer boundary of the first coordination shell. Once this clustering distance was set, we have run a GPU density based parallel scan (G-DBSCAN [62]) using an in-house code. Specific GPU optimizations were performed to calculate structure factors, pair distribution functions [63–65] and dynamic properties. Only clusters containing more than 4 particles have been considered for the analysis below.

A first observation from our cluster analysis is the fact that the structures are long-lived. In Figure 3 the average cluster life time, τ_{av} is displayed for the thermodynamics states under consideration. This quantity is defined as the average of the time a given cluster retains its identity (does not merge, split or dissolve, but it might incorporate/lose individual particles) in the course of the simulation. The top of the ordinate axis corresponds to the length of the production run, $\tau_{run} \approx 2700\tau_0$. For the highest density, up until $k_B T/\zeta = 15$ the average lifetime exceeds half the length of the simulation, which is an indication of the stability of the structures. This is explained by the large depth of the cluster-particle potential (see right graph of Figure 1). At $k_B T_c/\zeta \approx 15$ the clusters are extremely short lived, this temperature being fairly close to the limit of real solutions of the Hypernetted Chain integral equation, which has been discussed above. For higher temperatures no significant clustering is found. Now, when the density decreases the average life time of the clusters decreases substantially. The real solution of the HNC disappears at $k_B T/\zeta = 7.6$, but for $k_b T/\zeta = 9$ the simulation results still display a significant degree of clustering, although much more short lived. Simulation runs for higher temperatures (results not included) do not show evidence of clusters satisfying our minimum size criterion. In Figures S1 in the Supplementary

Information one can see snapshots of the evolution of the cluster formation as the system is cooled down from $k_B T/\zeta = 18$ to $k_B T/\zeta = 3$

As to the cluster statistics, in Figure 4 we present the cluster size distribution for the two densities in question and two selected temperatures (left graph) and the corresponding cluster radii distributions depicted in the right graph. As estimate of the cluster radii we have used the value of the gyration radius, which is defined in the usual fashion [66] by

$$R_g = \left\langle \sqrt{\frac{\sum_i m_i (\mathbf{r}_i - \mathbf{R}_{com})^2}{\sum_i m_i^2}} \right\rangle \quad (5)$$

where the brackets indicate an ensemble average and \mathbf{R}_{com} is the center of mass of the cluster whose radius of gyration is being computed. We see that for the largest density the size distribution peaks at around 450 particles and at 200 particles for the lowest. For all temperatures the clusters are liquid droplets, as will be shown below when analyzing the short time behavior of the mean square displacement.

Interestingly one can see that the shape of the cluster size distribution is hardly affected by temperature in the case of the largest density, whereas for low density becomes much wider and much larger clusters appear as temperature rises. This, in combination with the short lifetime of the clusters seen in Figure 3, is an indication of a rapid merging and splitting of clusters taking place for the lower density/high T case. The large spread of the low density-high T size distribution is also reflected in

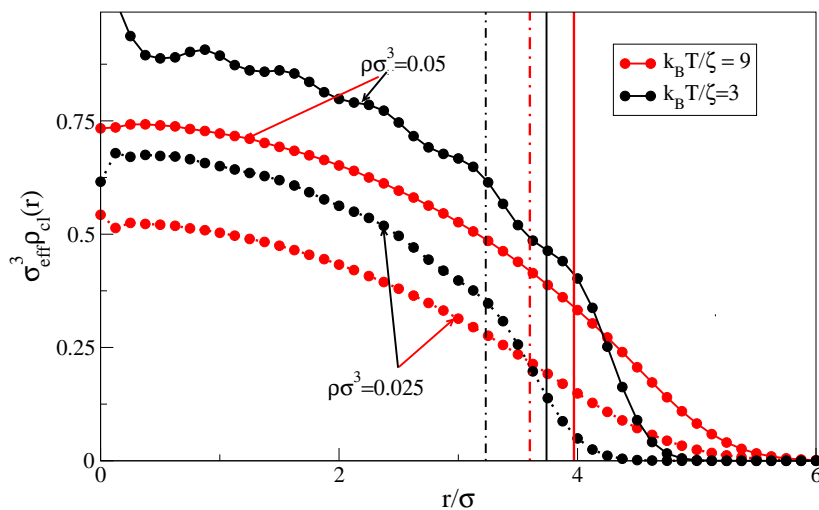


Figure 5. Temperature and density dependence of the average density profile of the clusters. Densities have been scaled with the effective diameter of the particles which is $\sigma_{eff} \approx 0.8\sigma$. Vertical lines denote the radii corresponding to the Gibbs dividing surface (cf. Eq. (6) in the text).

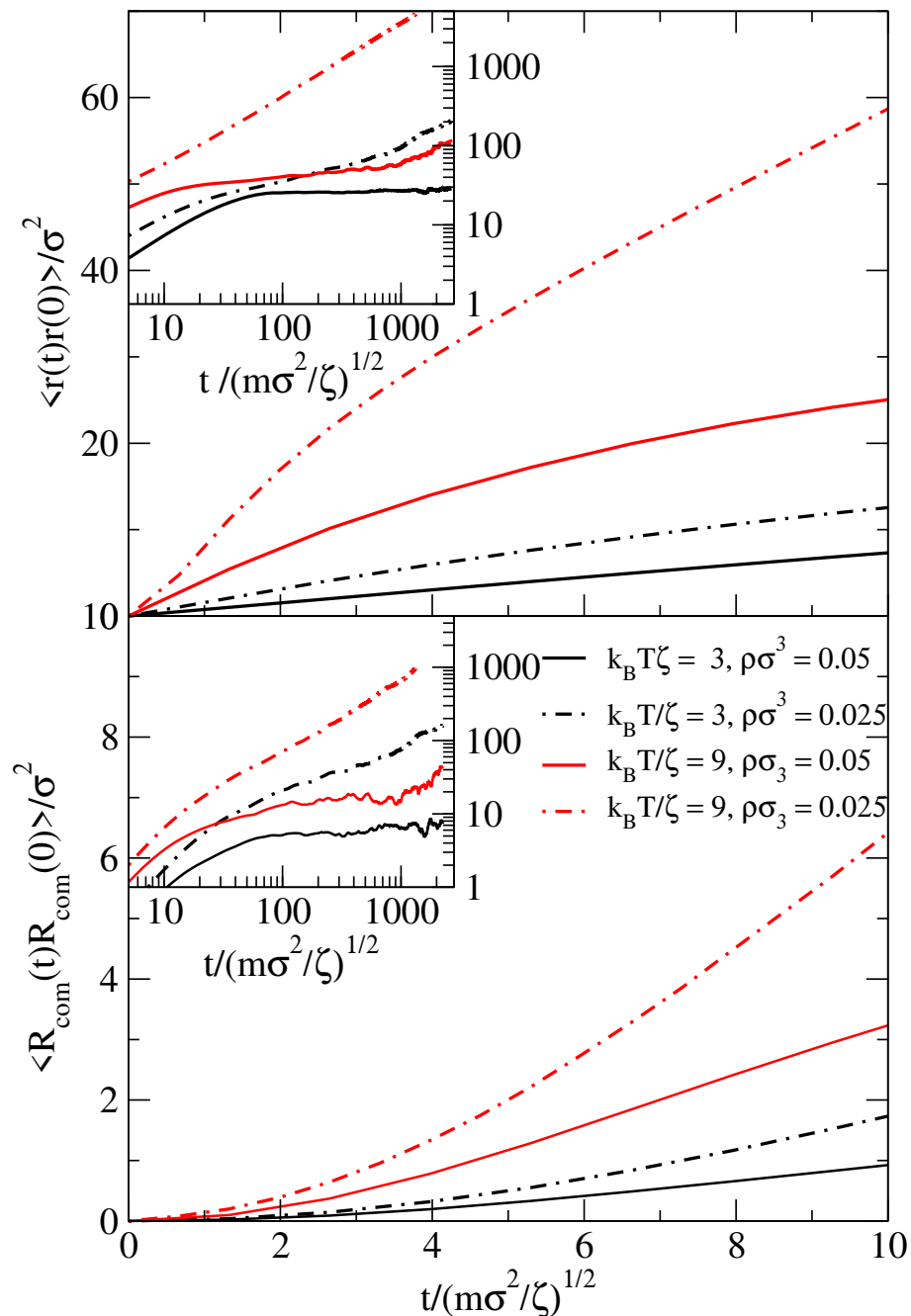


Figure 6. Upper graph) Single particle mean square displacement dependence of temperature and density. Lower graph) Density and temperature dependence of the center of mass mean square displacement for persistent clusters. In both graphs velocities and time are expressed in reduced units.

the cluster radii distribution, which in this case is almost Gaussian-like. All remaining distributions are negatively skewed beta-distributions with a more or less wide hump at approximately one particle diameter below the maximum of $P(R_g)$. Large clusters are in equilibrium with smaller ones, coalescing with them and letting particles escape their outer atmosphere to subsequently form smaller clusters. Merging of larger clusters is

prevented by the large intercluster repulsion (cf. see right graph of Figure 1), and this is at the root of the beta-distribution shapes. For the low density/high temperature case thermal energy is sufficient to overcome the intercluster repulsion to a certain extent, and the equilibrium between destruction and creation of clusters leads to a Gaussian-like distribution.

This picture is complemented by an inspection of the cluster average density profiles, $\rho_{cl}(r)$, depicted in Figure 5. In this case, we have scaled the densities with $\sigma_{eff} = 0.8\sigma$ in order to be able to compare the densities with those of standard fluids (e.g. for a Lennard-Jones fluid, liquid densities are usually assumed to be $\rho\sigma^3 \gtrsim 0.4$). One first notices that despite the extremely low total particle densities, for $\rho\sigma^3 = 0.05$ the clusters display very high values of the effective density profile, even for high T. These values are well into the liquid domain. For the lower global density, the effective inner cluster density remains practically within the boundaries of the liquid state. In both cases there is a transition towards gas-like densities as the profile approaches the surface in a gradual fashion. Taking into account that the clusters are rather spherical, we have defined a Gibbs dividing surface in order to have a quantitative description of the separation between gas-like particles and liquid-like particles, as is customary in the description of gas-liquid interfaces [58]. This surface places an ideal separation between the gas-like cluster region from its corresponding liquid-like counterpart. Here, for a spherical cluster this should be the surface of a sphere, whose radius (Gibbs dividing radius) R_{Gibbs} is given by

$$\int_0^{R_{Gibbs}} r^2(\rho_{cl}(0) - \rho_{cl}(r))dr = \int_{R_{Gibbs}}^{\infty} r^2\rho_{cl}(r)dr. \quad (6)$$

Obviously, when one has a uniform density, $\rho_{cl}(r) = \rho_{cl}(0)$ with a sharp interface at R_{Gibbs} , both sides of Eq. (6) are identically zero.

We see that these Gibbs radii separating gas-like and liquid-like particles in the clusters (vertical lines in Figure 5) follow the same trends as the average radii of gyration (vertical lines in Figure 4(b)), i.e. larger values for larger densities, and for the same density the radius increases with temperature. This latter trend reflects the larger spread of the cluster size distributions as temperature raises. The Gibbs radii are systematically larger ($\approx 0.5\sigma$) than the gyration radii. This is a consequence of the lesser weight of the “gas atmosphere” surrounding the quasi-spherical clusters in Eq. (5). It is worth noticing that the cluster density profiles reach vanishing values in the interval $4.5\sigma < r < 5.5\sigma$, by which the average cluster spatial extent is $\lesssim \lambda_0$. The temperature and density dependence of both R_{Gibbs} and R_g found in this paper agrees with the finding of Schwanzer et al. [46] for much smaller clusters in two dimensions.

Now a few words concerning the single particle dynamics. In what follows, in order to make the results independent of specific details of the model, time and frequency will be reduced with the corresponding molecular time unit, τ_0 and its inverse τ_0^{-1} respectively. Here we first look at the individual particle mean square displacement (m.s.d), plotted in the upper graph of Figure 6. It is apparent from the figure that there are clearly several separate regimes. First, there is a short time scale (under $2 \tau_0$, i.e.

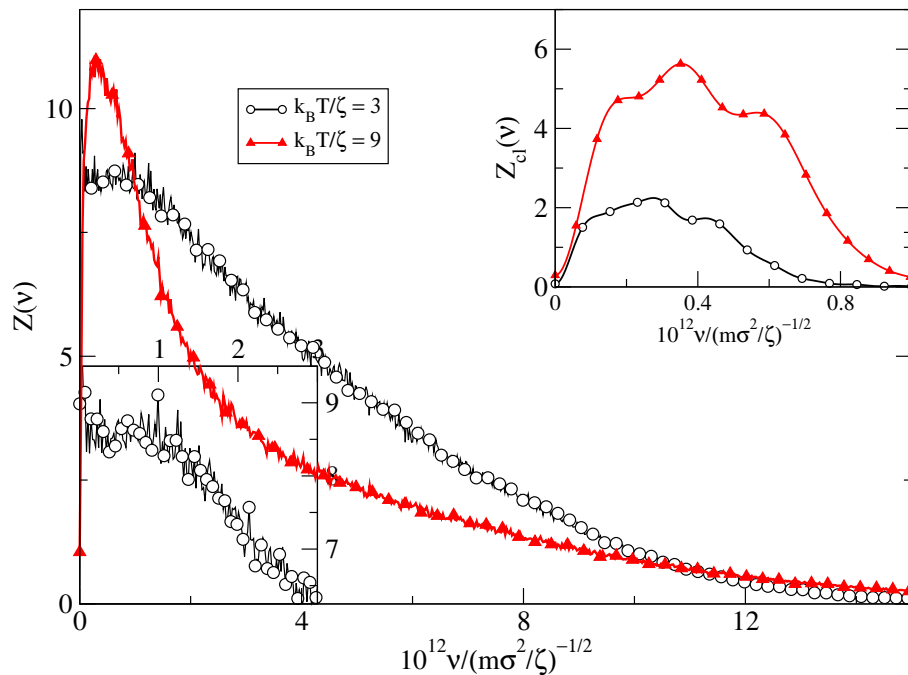


Figure 7. Vibrational frequency spectra derived from the particles velocity self-correlation at various temperatures and $\rho\sigma^3 = 0.05$, and the cluster vibrational frequency spectrum (inset in lower graph) as computed from the velocity self-correlation of the persistent clusters centers of mass.

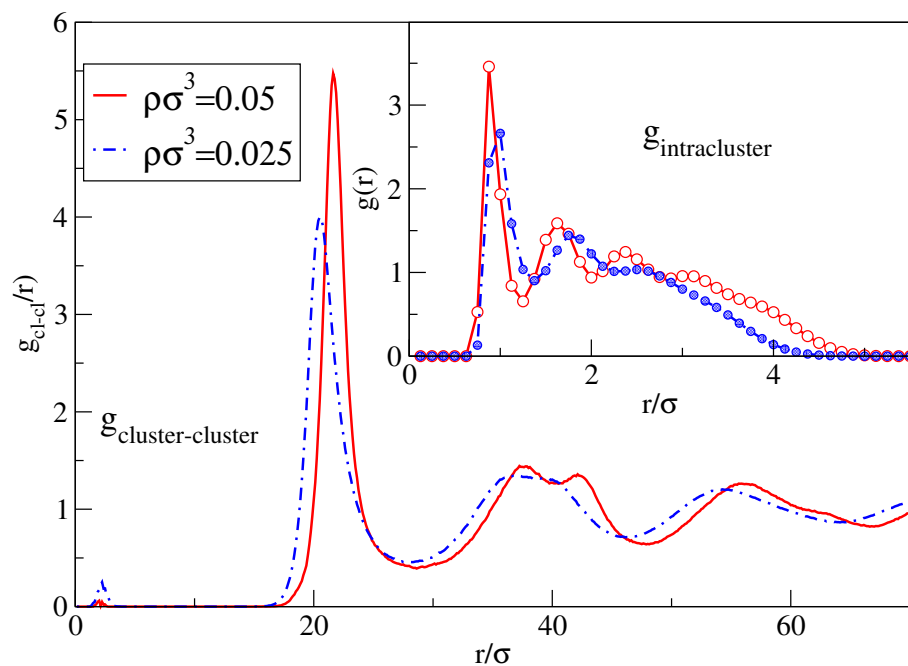


Figure 8. Cluster-cluster pair distribution function and intra-cluster pair distribution function (inset) for the lowest temperature state $k_B T / \zeta = 0.3$.

for our system around 14ps) where the system is in a diffusive regime corresponding to intracuster movements (the mean square displacement is $\lesssim 16\sigma^2 \approx \langle R_g^2 \rangle$). Then

the system reaches a subdiffusive regime with a decreasing diffusion constant (slope of the curves). This reflects the finite size of the clusters. For much longer times (up to $2.7 \times 10^3 \tau_0$) the behavior of the mean square displacement is represented in the inset. Now the low density-high temperature case displays a fully linear behavior in the m.s.d. in contrast with the other three instances. The two systems with the largest density display a plateau after the initial diffusive and subdiffusive regimes, which is then followed by a long time slightly diffusive behavior which is hardly apparent in the case of low T and highest density. This long time behavior stems from the collective cluster movement which is shown in the lower graph of Figure 6. Here we have plotted the mean square displacement of the center of mass of persistent clusters, that is, those that preserve their identity during the length of the production run, neither splitting nor merging with other clusters. At short times one can even appreciate the ballistic regime with a parabolic m.s.d. before the clusters begin to collide. We see that the long time behavior (inset) displays the same trends as the single particle mean square displacement, but one can actually measure a tiny diffusivity for the clusters at higher density/low temperature, namely $D/(\sigma^2 \zeta/m)^{1/2} = 0.0003$. This is an indication that our system is approaching an arrested glassy state, but there is still some remnant mobility. Taking into account that the source of this quasi-freezing of the cluster positions is mostly induced by the long range of the repulsive interactions (cf the right graph of Fig. 1) one is tempted to identify this state as a precursor of a Wigner glass of clusters [26]. However, strictly speaking the formation of Wigner crystals and glasses [67] is due to extremely long ranged interactions such a Coulombic ones, in conjunction with higher packing fractions. Following the discussion of Klix and coworkers [23] and bearing in mind the significant interparticle attraction and low packing fraction of our model, we are most likely somewhere near the dynamic transition towards a cluster glassy state.

These features are further confirmed by an analysis of the velocity self-correlation functions (cf. Figure S2 in the Supplementary Information). In all cases we see a significant “cage effect”, i.e. density is sufficiently high for the particles to reverse direction due to collisions with the nearest neighbors. For $k_B T/\zeta = 3$ and $\rho \sigma^3 = 0.05$, one can see the cage effect occurring within the cluster ($\tau_0 < 1$, m.s.d. $\ll R_g$). Already for the same T and $\rho \sigma^3 = 0.025$ one sees a second minimum at much larger times that can be ascribed to cluster dynamic correlations [46]. This cluster dynamics completely masks the single particle intracluster contribution in the high temperature cases, which is the reason why in these instance the “cages” encompass time ranges well above intracluster movements. Moving to the frequency domain, we see in Figure 7 that the high values of values of $Z(0)$ confirm the liquid-like dynamics of the constituent particles. For $k_B T/\zeta = 3$ and $\rho \sigma^3 = 0.05$, the cage effect vibrations reflect in a tiny maximum (see lower inset of Figure 7) observed at $10^{12} (m \sigma^2 / \zeta)^{1/2} \nu \approx 0.65$, whereas as T is increased a much wider maximum occurs at lower frequencies $10^{12} (m \sigma^2 / \zeta)^{1/2} \nu \approx 0.25$. This maximum stems from the coupled particle-cluster dynamics that is also seen in the velocity self-correlation function depicted in Figure S2. In the upper inset we have the corresponding vibrational frequency spectrum derived from the persistent cluster

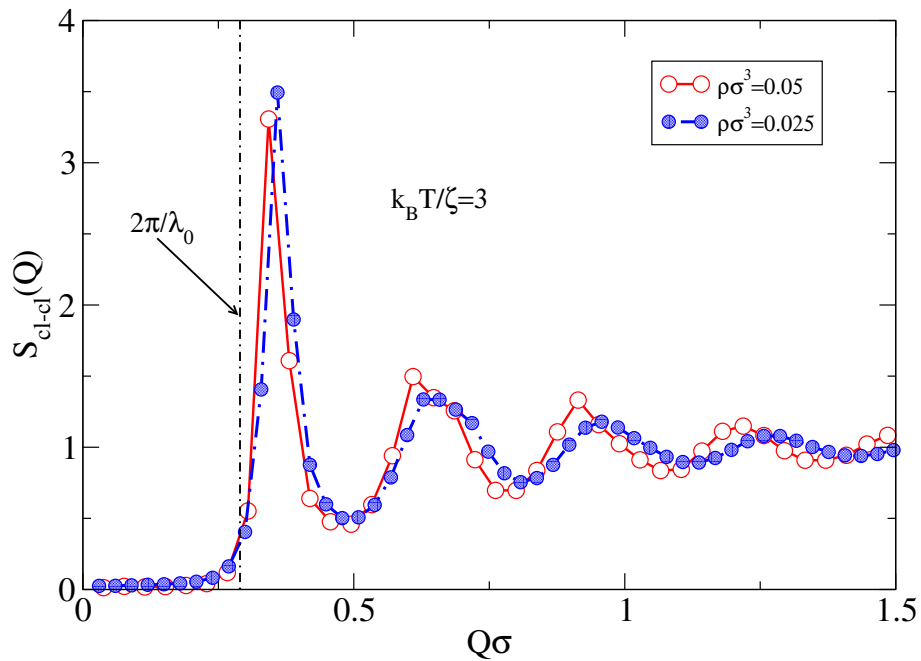


Figure 9. Cluster-cluster structure factor for the lowest temperature state, $k_B T/\zeta = 0.3$.

velocity self-correlation function. Now the situation is completely different and the low frequency behavior corresponds to a that of a system approaching a glassy state, with very low diffusivities ($Z_{cl}(0) \rightarrow 0$), in agreement with the long time behavior of the m.s.d. seen in Figure 6. Note that the frequency domain of the cluster dynamics is one order of magnitude smaller than that of single particles, reflecting the much slower dynamics of the clusters, a consequence of their large masses. The intensity of the peaks increases with temperature, as the kinetic energy increase reflects mostly in more intense vibrations around equilibrium positions, with the maxima shifting to slightly higher energies. This three maxima correspond to three minima (cages) in the cluster velocity self-correlation function (right graph in Figure S2), where also one can see that the cages become narrower and move to shorter times as temperature is increased. This effect stems from the higher vibrational energy present in the high T state, which at $\rho\sigma^3 = 0.05$ still preserves some of the characteristics of a quasi-amorphous state. Lowering the density and/or further increasing the temperature above $k_B T/\zeta > 15$ obviously ends up in the dissociation of the clusters and the disappearance of the vibrational structure of the spectrum.

5. Two-particle and intercluster structural correlations. Build-up of effective hyperuniformity

We can now analyze two-particle correlations. To start with, in Figure 8 we present the cluster-cluster pair distribution function for the lowest temperature and the two densities under consideration. In the inset the corresponding particle-particle intracluster pair

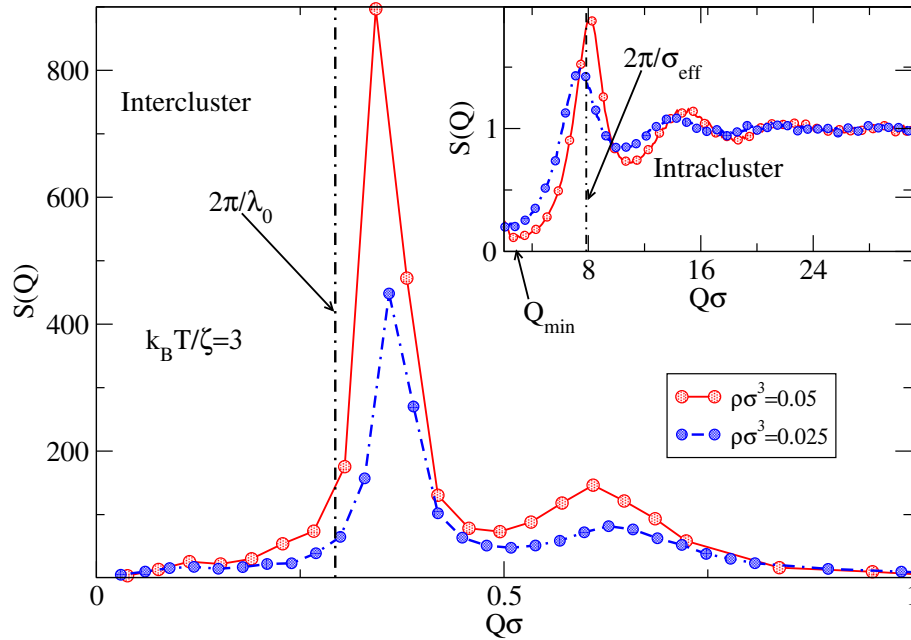


Figure 10. Temperature and density dependence of the total structure factor $S(Q)$ (main graph) and the intracuster structure factor (inset) for the system in stable cluster phases.

distribution functions are shown. Our previous discussion concerning the average intercluster potential (cf. right graph in Figure 1) explains that clusters are separated by the correlation length $\lambda_0 \approx 20\sigma$. The smaller size of the clusters for low density implies the shift of the first peak of $g_{cl-cl}(r)$ to lower distances. The splitting of the second coordination shell for $\rho\sigma^3 = 0.05$ is a typical signature of the presence of an amorphous structure [52], although in our case there is a residual diffusivity. Interestingly, this feature is found in dense amorphous systems, but in contrast here, the total density is very low ($\rho\sigma^3 = 0.05$). Nonetheless, we must bear in mind that the excluded volume of the clusters is much larger than what would correspond to their actual size, as previously discussed. Thus, for instance, Figure 8 is obtained from a total of $N_{cl} \approx 500$ clusters in a cubic box of side $L=165\sigma$. If one uses as rough estimate of the effective cluster diameter the position of the first maximum of g_{cl-cl} , $\sigma_{cl}^{eff} \approx 20\sigma$, the effective density of clusters is $N_{cl}\sigma_{cl}^{eff3}/L^3 \approx 0.9$ which is certainly high. As we have seen, the effective diameter is approximately twice the spatial extent of the clusters, due to the long range repulsion of the effective cluster-cluster interaction, as seen in the right graph of Figure 1. On the other hand, once the density is halved the splitting disappears and the system becomes more liquid-like, even if the cluster diffusivity remains relatively low ($D/(\sigma^2\zeta/m)^{1/2} = 0.006$).

As to the intracuster pair distribution function, its decay beyond 3σ is a consequence of the finite averaged cluster size (cf the density profiles of Figure 5) but its liquid-like structure is very remarkable, with a first coordination shell reaching considerably high values. From the position of the first peaks and their decay towards

shorter interparticle separations, one can appreciate that the potential core is relatively soft, and that is the reason why we have considered an effective particle diameter $\sigma_{eff} \approx 0.8\sigma$. A steeper repulsion in Eq. (1) (e.g. a Lennard-Jones r^{-12} term) would bring the effective size closer to σ , but this would require a finer grid in the potential interpolation used in the LAMMPS package [57] which might lead to memory exhaustion in the GPUs.

If we now move from real to Fourier space, in Figure 9 we have the cluster-cluster structure factor, $S_{cl-cl}(Q)$. A first feature is to be noted, the height of the first peak for both densities is beyond Hansen-Verlet's [68] freezing rule $S(Q_m) \gtrsim 2.86$ for which a transition towards a crystal is to be expected. As discussed above, our system presents features of an amorphous solid, but with a somewhat peculiar structure factor. We see that $S(Q) \approx 0, \forall Q \lesssim 0.2\sigma^{-1}$. In fact, one finds that the hyperuniformity index $H = S(Q_{max})/S(0 < Q \lesssim 0.2\sigma^{-1}) \approx 10^3 \sim 10^2$ is relatively high. While this value is still away from the criterion for *near hyperuniformity*, $H \gtrsim 10^4$ proposed by Atkinson and coworkers [69] in maximally random jammed systems, it represents a considerable attenuation of density fluctuations, and actually meets the criterion of *effective hyperuniformity*, $H \gtrsim 10^2$ proposed by Chen and et al. [70]. Lowering the temperature and choosing a material with the appropriate scattering form factor will improve the hyperuniform and stealthy character of the material for wavenumbers below $0.2\sigma^{-1}$. Tuning the size of the constituent particles one could increase or decrease the wavenumber range of stealthiness.

We note that the positions of the first maximum of the structure factors deviate from the value estimated from the correlation length, $Q_m = 2\pi/\lambda_0$ (shown in the Figure by a vertical line), almost by 20%. Although the first peak of the intercluster pair distribution (Fig. 8) appears at $\approx \lambda_0$, the real effective cluster-cluster interaction is much softer than that depicted in the right graph of Figure 1. The particle density inside the clusters (cf. Figure 5) is far from the uniform density that was assumed in Eq. (4). This should lead to a softer outer range of the intercluster effective potential explaining the shift of Q_m with respect to $2\pi/\lambda_0$. The fact that $Q_m(\rho\sigma^3 = 0.05) > Q_m(\rho\sigma^3 = 0.025)$ reflects the smaller size of the clusters for the lower density (see the corresponding radii of gyration in Figure 4(b)) and matches the shift to lower r of the first maximum of g_{cl-cl} in Figure 8.

If we now look at the total structural factor, $S(Q)$ depicted in Figure 10, its most noticeable feature is the huge magnitude of the prepeak, which is the signature of a large degree of clustering. Obviously the prepeak positions correspond to that of the first maxima in the cluster-cluster structure factors discussed above. Also here the hyperuniformity index meets the criterion of *effective hyperuniformity*.

In the inset we can see the large wavenumber behavior of $S(Q)$. The peak maxima $Q_{max}\sigma \approx 8.1$ reflects interparticle correlations at 0.8σ , which is precisely the effective particle diameter, σ_{eff} . This is in accordance with the maxima of $g(r)$ in the inset of Figure 8. Interestingly, $H = S(Q_{max})/S(Q_{min}) = 0.2 \times 10^2$ which is not very far from the criterion of effective hyperuniformity. A proper choice of the short range interparticle

interactions might actually drive the system closer to having an additional wavenumber range where density fluctuations should be heavily attenuated.

In order to further confirm the effective hyperuniform character of our systems we have analyzed the local density (or particle number) fluctuations, defined as

$$\sigma_N^2(R) = \langle N^2 \rangle_R - \langle N \rangle_R^2 \quad (7)$$

where N refers to the number of particles and the subscript R refers to a sampling volume, in this case a sphere of radius R . This quantity is known to fulfill [31] $\sigma_N^2(R) = \langle N \rangle_R$ for a Poisson point pattern, which epitomizes a completely random disordered and uncorrelated system. In fact, in many disordered cases $\sigma_N^2(R) \propto R^d$, where d is the dimensionality. At the other end of the story, one has point patterns known as *hyperuniform* that fulfill $\sigma_N^2(R) \propto R^{d-\alpha}$, among which one finds regular patterns such as those of crystals and quasicrystals for which $\alpha = 1$ [31]. Other intermediate cases exist (e.g. with logarithmic scaling), with the term *strong hyperuniformity* reserved for those systems in which $\alpha \geq 1$ [71]. Back to our problem, in Figure 11 we present the corresponding analysis based on the configurations of the clusters' center of mass. The number fluctuation is computed averaging both the number of clusters, N_{cl} and N_{cl}^2 for sample spheres of radius R randomly placed in the simulation box. Note that particle number fluctuations are strongly affected by the periodic nature of our sample, since sampling over r-space is limited in accuracy by the Fourier space constraint that must be satisfied in the presence of periodic boundary conditions, namely, $\mathbf{Q} = (n_x, n_y, n_z)2\pi/L$, where n_i are integer numbers and L is the side of the simulation box. For this reason, local number fluctuation can only be accurately computed for values well below half the simulation box size, otherwise effects of the periodic nature of the sample become visible. These limitations have been analyzed in detail by Wright in Ref. [72].

Now, in the left graph of Figure 11, one observes that $\sigma_{N_{cl}}^2(R) \propto R^2$ except for the high temperature/low density case. The curves exhibit strong oscillations, evenly distributed around the linear regression lines (dotted lines in the figure), and indicate that the system has strong spatial correlations consistent with a dense amorphous system. On the right graph the scaled ratio $\sigma_N^2(R)/(4\pi n_{cl}R^3/3)$ is displayed vs the radius of the sampling sphere, R . Here $n_{cl} = \langle N_{cl} \rangle / L^3$ is the average density of clusters. A decreasing trend in the R -dependence of this ratio is a signature of hyperuniformity [32]. Both graphs of Figure 11 indicate that our systems (with the exception of the low density/high T case) display inter-cluster structures that can be deemed *effective hyperuniform* from the point of view of number (or local density) fluctuations. When the right graph of Figure 11 is compared with Figure 2 of Ref. [32], we can clearly appreciate that our systems are somewhere in between ordered and disordered hyperuniform point configurations, as could be expected from a glassy-like system. The same analysis can be performed on particle number fluctuations. These results are presented in similar graphs in Figure S3 of the Supplementary Information. Now the oscillations of $\sigma_N^2(R)$ are much more pronounced, reflecting the fact the the sample sphere of radius R crosses the boundaries of dense clusters to then sample almost

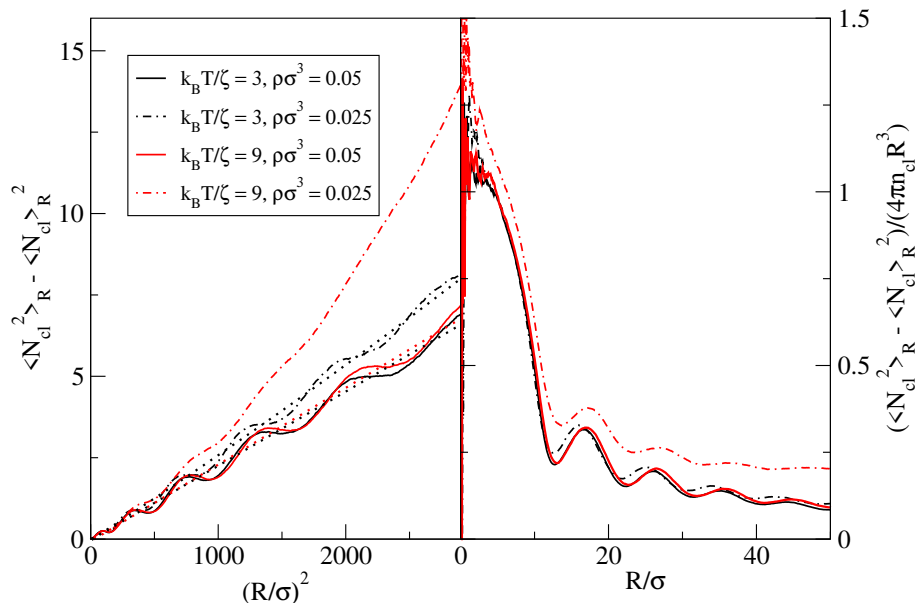


Figure 11. Left) Local particle number variation of cluster center of mass configurations vs the sample sphere radius squared, R^2 . The linear dependence is an indication of a hyperuniform configuration. Deviation in linearity is apparent in the high T/low density case. Dotted lines represent linear regressions to the simulation data. Right) Local particle number variation of cluster center of mass configurations scaled with the corresponding random uniform value, $4\pi n_{cl} R^3/3$ vs the sample radius, R . A decaying trend indicates the presence of a disordered hyperuniform system. Again, for the high T/low density case the scaled number fluctuation tends to remain constant.

empty space. Nonetheless, now in all cases curves display a rather linear dependence on R^2 . Also, the scaled number fluctuations $\sigma_N^2(R)/(4\pi\rho R^3/3)$ in all cases exhibit an overall decreasing dependence with R . One might infer that from the point of view of particle configurations, all systems studied can be cast into the class of *effectively hyperuniform* materials.

6. Conclusions

In summary, we have presented a study of the structural and dynamic properties of a simple model of a type-III SALR self-associating fluid, focusing on the globular cluster phase that upon aggregation displays effective hyperuniform disorder. Here we have studied both cluster size distributions, cluster density profiles, diffusion and frequency spectra as well as pair distributions (inter and intracluster) and structure factors. From the latter, we have found that the cluster phase for moderate densities (but still low packing fraction) approaches a cluster glassy state. In these conditions the system shows a considerable attenuation of density fluctuations for a range of wavenumbers below $0.2\sigma^{-1}$, meeting the criteria of *effective hyperuniformity and stealthiness*. Letting aside the influence of particle form factors which also play a fundamental role, for large

colloidal particles ($\sigma \approx 1 \sim 10\mu\text{m}$), attenuation would take place for radiation in the low frequency range of radio waves. The region of interest can be tuned resorting to mixtures of cluster-forming particles [70] and/or controlling the size of the clusters. Future work will focus on mixtures where intracuster phase separation can enable the tuning of anisotropic cluster-cluster interactions and systems in which self-limitation is controlled by saturation of associative sites.

Acknowledgments

The authors acknowledge the support from the Agencia Estatal de Investigación and Fondo Europeo de Desarrollo Regional (FEDER) under grants No. PID2020-115722GB-C21 and PID2020-115722GB-C22. We also would like to acknowledge the Galicia Supercomputing Center (CESGA) for the access to their computer facilities.

- [1] Stradner A, Sedgwick H, Cardinaux F, Poon W C K, Egelhaaf S U and Schurtenberger P 2004 *Nature* **432** 492 – 495
- [2] Ciach A, Pekalski J and Gozdz W T 2013 *Soft Matter* **9** 6301
- [3] Liu Y, Porcar L, Chen J, Chen W R, Falus P, Faraone A, Fratini E, Hong K and Baglioni P 2010 *The Journal of Physical Chemistry B* **115** 7238–7247
- [4] Yearley E, Godfrin P, Perevozchikova T, Zhang H, Falus P, Porcar L, Nagao M, Curtis J, Gawande P, Taing R, Zarraga I, Wagner N and Liu Y 2014 *Biophys. J.* **106** 1763–1770
- [5] Kovalchuk N, Starov V, Langston P and Hilal N 2009 *Adv. Colloid Interfac.* **147–148** 144–154
- [6] Sweatman M B and Lue L 2019 *Advanced Theory and Simulations* **2** 1900025
- [7] Hirose T, Ninomiya K, Nakagawa S and Yamazaki T 2022 *Nat. Rev. Mol. Cell Biol.* **24** 288–304
- [8] Murthy A C and Fawzi N L 2020 *Journal of Biological Chemistry* **295** 2375–2384
- [9] Sear R P, Chung S W, Markovich G, Gelbart W M and Heath J R 1999 *Phys. Rev. E* **59** R6255
- [10] Boles M A, Engel M and Talapin D V 2016 *Chemical Reviews* **116** 11220–11289
- [11] Barad H N, Kwon H, Alarcón-Correa M and Fischer P 2021 *ACS Nano* **15** 5861–5875
- [12] Andelman D, Broçhard F and Joanny J F 1987 *The Journal of Chemical Physics* **86** 3673–3681
- [13] Seul M and Andelman D 1995 *Science* **267** 476–483
- [14] Archer A J, Pini D, Evans R and Reatto L 2007 *J. Chem. Phys.* **126** 014104
- [15] Mossa S, Sciortino F, Tartaglia P and Zaccarelli E 2004 *Langmuir* **20** 10756–10763
- [16] Liu Y and Xi Y 2019 *Current Opinion in Colloid & Interface Science* **39** 123–136
- [17] Archer A J 2008 *Phys. Rev. E* **78** 031402
- [18] Archer A J, Ionescu C, Pini D and Reatto L 2008 *J. Phys.: Condens. Matter* **20** 415106
- [19] Bomont J M, Bretonnet J L, Costa D and Hansen J P 2012 *J. Chem. Phys.* **137** 011101
- [20] Bomont J M and Costa D 2012 *J. Chem. Phys.* **137** 164901
- [21] Sweatman M B, Fartaria R and Lue L 2014 *J Chem Phys.* **140** 124508
- [22] Archer A J and Wilding N B 2007 *Phys. Rev. E* **76** 031501
- [23] Klix C L, Royall C P and Tanaka H 2010 *Physical Review Letters* **104** 165702
- [24] Godfrin P D, Valadez-Pérez N E, Castañeda-Priego R, Wagner N J and Liu Y 2014 *Soft Matter* **10** 5061 – 5071
- [25] Zhuang Y and Charbonneau P 2016 *J. Phys. Chem. B* **120** 6178–6188
- [26] Ruiz-Franco J and Zaccarelli E 2021 *Annu. Rev. Condens. Ma. P.* **12** 51–70
- [27] Palaia I and Šarić A 2022 *J. Chem. Phys.* **156** 194902
- [28] Bosse J and Wilke S D 1998 *Phys. Rev. Lett.* **80** 1260–1263
- [29] Dawson K A 2002 *Current Opinion in Colloid & Interface Science* **7** 218–227
- [30] Weitz D A 2011 *Glasses and grains* (Birkhauser) chap Colloidal Glasses, pp 25–38
- [31] Torquato S and Stillinger F H 2003 *Phys. Rev. E* **68** 041113

- [32] Torquato S 2018 *Phys. Rep.* **745** 1–95
- [33] Florescu M, Torquato S and Steinhardt P J 2009 *Proceedings of the National Academy of Sciences* **106** 20658i – 20663
- [34] Florescu M, Torquato S and Steinhardt P J 2009 *Phys. Rev. B* **80** 15512
- [35] Froufe-Pérez L S, Engel M, Sáenz J J and Scheffold F 2017 *Proc. Natl. Acad. Sci. U.S.A.* **114** 9570–9574
- [36] Zhou W, Tong Y, Sun X and Tsang H K 2019 *ArXiv*
- [37] Milošević M M, Man W, Nahal G, Steinhardt P J, Torquato S, Chaikin P M, Amoah T, Yu B, Mullen R A and Florescu M 2019 *Scientific Reports* **9**
- [38] Romero-García V, Lamothe N, Theocharis G, Richoux O and García-Raffi L 2019 *Physical Review Applied* **11** 054076
- [39] Chéron E, Groby J P, Pagneux V, Félix S and Romero-García V 2022 *Physical Review B* **106** 064206
- [40] Imperio A and Reatto L 2004 *J. Phys.: Condens. Matter* **16** S3769–S3789
- [41] Imperio A and Reatto L 2006 *J. Chem. Phys.* **124** 164712
- [42] Imperio A, Pini D and Reatto L 2006 *International Workshop on Collective Phenomena in Macroscopic System* (Villa Olmo, Como, Italy) URL <http://arxiv.org/abs/cond-mat/0703060>
- [43] Imperio A and Reatto L 2007 *Phys. Rev. E* **76** 040402(R)
- [44] Kac M 1959 *Phys. Fluids* **2** 8–12
- [45] Schwanzer D F and Kahl G 2010 *J. Phys. : Condens. Matter* **22** 415103
- [46] Schwanzer D F, Coslovich D and Kahl G 2016 *J. Phys. Condens. Matter* **28** 414015
- [47] Lomba E, Bores C and Kahl G 2014 *J. Chem. Phys.* **141** 164704
- [48] Bores C, Almarza N, Lomba E and Kahl G 2015 *J. Phys. : Condens. Matter* **27** 194127
- [49] Meyra A G, Zarragoicoechea G J and Kuz V A 2012 *Mol. Phys.* **110** 173 – 178
- [50] Meyra A G, Zarragoicoechea G J and Kuz V A 2015 *Physical Review E* **91** 052810
- [51] Illing B, Fritschi S, Kaiser H, Klix C L and Georg Maret n P K 2017 *Proc. Natl. Acad. Sci. U.S.A.* **114** 1856
- [52] Pan S P, Qin J Y, Wang W M and Gu T K 2011 *Physical Review B* **84** 092201
- [53] Batten R D, Stillinger F H and Torquato S 2008 *J. Appl. Phys.* **104** 033504
- [54] Morse P K, Kim J, Steinhardt P J and Torquato S 2023 *Phys. Rev. Research* **5** 033190
- [55] Kac M, Uhlenbeck G E and Hemmer P C 1963 *J. Math. Phys.* **4** 216
- [56] McGreevy R L 2001 *J. Phys.: Condens. Matter* **13** R877–R913
- [57] Thompson A P, Aktulga H M, Berger R, Bolintineanu D S, Brown W M, Crozier P S, in 't Veld P J, Kohlmeyer A, Moore S G, Nguyen T D, Shan R, Stevens M, Tranchida J, Trott C and Plimpton S J 2021 *Comput. Phys. Commun.* **271** 108171
- [58] Hansen J P and McDonald I 2006 *Theory of simple liquids* 3rd ed (Academic Academic Press)
- [59] Lomba E and López-Martín J L 1995 *J. Stat. Phys.* **80** 825–840
- [60] Stell G 1995 *Journal of Statistical Physics* **78** 197–238
- [61] Bollinger J A and Truskett T M 2016 *J Chem. Phys.* **145** 064902
- [62] Andrade G, Ramos G, Madeira D, Sachetto R, Ferreira R and Rocha L 2013 *Procedia Computer Science* **18** 369–378
- [63] Levine B G, Stone J E and Kohlmeyer A 2011 *J. Comput. Phys.* **230** 3556–3569
- [64] Sakharnykh N 2015 Gpu pro tip: Fast histograms using shared atomics on maxwell Tech. rep. NVIDIA Corporation URL <https://developer.nvidia.com/blog/gpu-pro-tip-fast-histograms-using-shared-atomics-maxwell/>
- [65] Reuter K and Köfinger J 2019 *Computer Physics Communications* **236** 274–284
- [66] 2006 *IUPAC Compendium of Chemical Terminology* chap Radius of Gyration 3rd ed
- [67] Duang F and Guojun J 2005 *Introduction to Condensed Matter Physics* vol I (Singapore: World Scientific)
- [68] Hansen J P and Verlet L 1969 *Phys. Rev.* **184** 151 – 161

- [69] Atkinson S, Zhang G, Hopkins A B and Torquato S 2016 *Physical Review E* **94** 012902
- [70] Chen D, Lomba E and Torquato S 2018 *Phys. Chem. Chem. Phys.* **20** 17557–1 7562
- [71] Oğuz E C, Socolar J E S, Steinhardt P J and Torquato S 2017 *Phys. Rev. B* **95** 054119–1
- [72] Wright A C 2017 *J. Non-Cryst. Solids* **461** 113–128